Journal of Materials Chemistry C

Exciton Energy Transfer in Organic Light Emitting Diodes with Thermally Activated Delayed Fluorescence Dopants

Journal:	*Journal of Materials Chemistry C*
Manuscript ID	TC-ART-04-2018-001992.R1
Article Type:	Paper
Date Submitted by the Author:	07-Jun-2018
Complete List of Authors:	Lyskov, Igor; RMIT University, ARC Centre of Excellence in Exciton Science, School of Science Etinski, Mihajlo; University of Belgrade, Faculty of Physical Chemistry Marian, Christel; Heinrich-Heine-Universität, Chemsitry, Theor. Chemsitry Russo, Salvy; RMIT University, Applied Physics

Journal Name

ARTICLE TYPE

Cite this: DOI: 10.1039/xxxxxxxxxx

Exciton Energy Transfer in Organic Light Emitting Diodes with Thermally Activated Delayed Fluorescence Dopants†

Igor Lyskov,*[a] Mihajlo Etinski,[b], Christel M. Marian[c] and Salvy P. Russo[a]

Received Date
Accepted Date

DOI: 10.1039/xxxxxxxxxx

www.rsc.org/journalname

The molecular systems exhibiting thermally activated delayed fluorescence (TADF) are widely used as fluorescent dopants in organic light-emitting diodes (OLED) due to their capacity to harvest triplet excitons. The optoelectronic properties of a TADF-based OLED can be further improved by co-depositing highly luminescent fluorophore into emissive layer. In a double-dopant architecture the electrically generated excitons on TADF molecules are transmitted to the fluorescent emitter for radiative recombination. In this theoretical study we investigate the ability of the singlet excitons on PXZ-TRZ for non-radiative hoping to Rubrene by varying ambient temperature and solvent polarity. The non-zero probability of the exciton energy transfer is attributed to vibronic interaction between the charge-transfer (CT) and optically bright high-lying states on TADF monomer. We systematically extend the outcome of our calculations on the similar class of dimers and discuss how the preferential orientation of linear shaped TADF molecules and their complementary fluorophores can enhance efficiency of energy transfer.

1 Introduction

Low-dimensional purely organic molecular semiconductors, exhibiting TADF upon an annihilation of electron-hole pairs have proven to be very efficient light-emitting systems utilized in an electronic device such as OLEDs [1–8]. Their electroluminescence properties, low fabrication cost, high flexibility for molecular design make them excellent candidates for future generation displays. An enhancement of the conventional 25% of internal quantum efficiency stems from the molecular ability to undergo a spin-forbidden reverse intersystem crossing (rISC) reaction [9–12]. Thereby, up to 100% of all excitons can be utilized for light generation. However, the degradation mechanisms are currently limiting the OLEDs performance. [13]

The OLEDs degradation is commonly attrubited to intermoleculat triplet-polaron annihilation (TPA) and triplet-triplet annihilation (TTA). [13–17] The former quenches the excited state on a dopant and transmits its energy to a charged host molecule producing a high-energy polaron. The latter forms delocalized biexcitons with statistically stipulated spin states and with twice the energy of the parent intramolecular triplet. The aforementioned biexcitons lie energetically well above the charge carrier energy, and can be turned into a hot polaron burning subtle organic systems. Another spin-forbidden process of singlet-triplet annihilation (STA) can also contribute to exciton quenching in TADF-based OLED [18,19]. The suppression of the exciton-polaron annihilation, supervening the collision of two Frenkel-type excitons, was shown to be an effective way to increase operational life-time of ordinary single-dopant rISC-based OLED materials [13,18,20–23].

One of the approaches to systematically reduce efficiency roll-off in OLEDs rests on the idea of suppressing intersystem crossing (k_{ISC}) and fluorescence from TADF center (k_F) by a fast channel of singlet exciton energy transfer (ET) to highly fluorescent molecules. [24–26]. In this double-dopant architecture, the TADF molecule does not luminesce itself but serves as an exciton sensitizer and non-radiatively transfers (k_{ET}) its singlet excitation energy to a fluorophore for radiative recombination, also known as hyperfluorescence (k_{HF}). Zhang et al. [27] showed advantages of the strategy using the sensitizing TADF materials with small singlet-triplet gap in the ET processing device. Nakatonani et al. [24] embedded different aromatic compounds at low concentration in a host-guest system to produce blue, green, yellow and red light. They found that the use of electrochemically stable fluorescent dopants in combination with TADF sensitizers provides significant enhancement of operational stability of a device

[a] Chemical and Quantum Physics Group, ARC Centre of Excellence in Exciton Science, School of Science, RMIT University, Melbourne, 3000, Australia. Fax: +61 3 9926 5290; Tel: +61 3 9925 1647; E-mail: igor.lyskov@rmit.edu.au
[b] Faculty of Physical Chemistry, University of Belgrade, Studentski trg 12-16, 11000 Belgrade, Serbia.
[b] Institute of Theoretical and Computational Chemistry, Heinrich Heine University Düsseldorf, Universitätsstr. 1, D-40225 Düsseldorf, Germany.

† Electronic Supplementary Information (ESI) available: computational details of the energy transfer rate, transition dipole derivatives, thermal vibrational density and ML-MCTDH setup. See DOI: 10.1039/b000000x/

Fig. 1 Chemical structure of PXZ-TRZ and Rubrene and schematic process of the exciton transfer. Red and blue colors refer to the constituent electron and hole density localization of excitons, respectively.

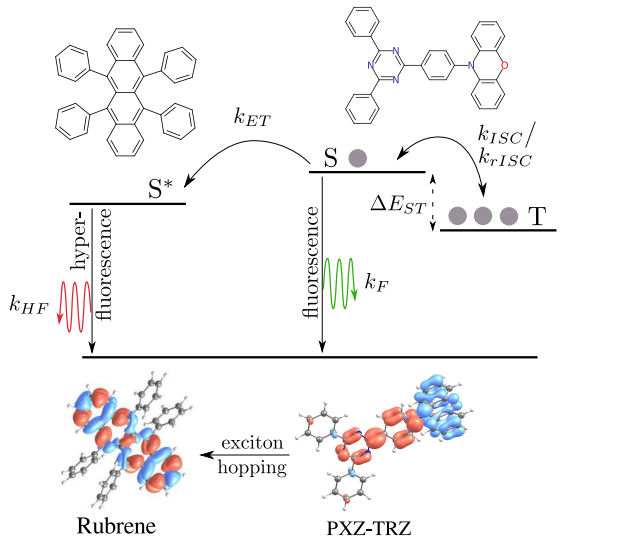

while maintaining high electroluminescence efficiency. Utilizing a phosphorescent molecule as the singlet energy acceptor and TADF molecule as energy donor, Fukagawa et al.[26] found that the operational lifetime of phosphorescence devices is nearly proportional to the ET rate.

Considering STA, TTA and TPA exclusively as dissipation channels in a E-type fluorescence device, the singlet $[S]$ and triplet $[T]$ state populations in TADF can be written as,

$$\frac{d[S]}{dt} = -k_F[S] - k_{ET}[S] - k_{ISC}[S] + k_{rISC}[T] - k_{STA}[S][T] \quad (1)$$

$$\frac{d[T]}{dt} = -k_{rISC}[T] + k_{ISC}[S] - \left(k_{TTA}[T]^2 + k_{TPA}[T][X] + k_{STA}[S][T]\right) \quad (2)$$

$$\frac{d[S^*]}{dt} = k_{ET}[S] - k_{HF}[S^*] \quad (3)$$

where $[S^*]$ and $[X]$ denote population of a fluorophore and polaronic state correspondingly. An evaluation of the k_{TTA}, k_{TPA} and k_{STA} rates represents a big computational challenge, and we do not quantitatively consider them in this work. As seen from the above written equations, the triplet states are subjected to bimolecular reactions entailing efficiency roll-off more severe than singlets. Therefore, reducing their transient lifetime can help to rule out biexciton and hot polaron formation problems to some extent. This can be achieved through enhancing k_{ET}. An enhancement of the k_{ET} rate constant can be achieved by optimizing the relative orientation of the ET partners[28,29]. A rapid depletion of the singlet density owing to the exciton transfer inevitably influences the spin-vibronic dynamics in TADF facilitating triplet-to-singlet upconversion according to Equations 1,2,3.

In this paper we predict theoretically how singlet exciton energy transfer can be enhanced by controlling the mutual orientation of OLED dopants. Using the energy donor *2,4,6-tri(4-(10H-phenoxazin-10H-yl)phenyl)-1,3,5-triazine*, hereinafter referred to as PXZ-TRZ, and the energy acceptor *(5,6,11,12-tetraphenyltetracene)*, referred to as Rubrene, we investigate the ability of the singlet exciton in PXZ-TRZ for non-radiative hopping to Rubrene (Figure 1). Using various solvents and ambient temperature regimes we calculate a critical interchromophore distance, known as Förster radius, at which an excitonic coupling between the monomers is strong enough to suppress TADF luminescence and to substantially reduce singlet-to-triplet conversion. Although, the emissive CT state does not possess an electronic transition dipole in the Condon approximation, we will explain that the rate of the exciton transfer from the TADF molecule is a vibrationally stipulated quantity and that the transfer can be mitigated by spatial alignment of exciton donor and exciton acceptor in a double-dopant device.

2 Computational details

The ground S_0 and excited S_1 state geometries of PXZ-TRZ and Rubrene were obtained with the Turbomole package[30], employing density functional theory (DFT) with the semilocal BHLYP exchange-correlation functional[31] and the valence split atomic orbital basis set def-SV(P)[32]. Due to the close distance between phenyl rings in Rubrene, we have accounted for dispersion interaction by means of D3-BJ dispersion correction[33] in the geometry optimizations. Vibrational frequencies and normal displacement vectors of the monomers were obtained numerically with the SNF software[34] at the same level of theory as above. The corrected linear response approach to the polarizable continuum model PisaLR[35] treats electrostatic interaction between the state-specific molecular density and polarizable environment, and defines the excited-state energy shifts and the interchromophore coupling in different solvents. The effective PisaLR point charges on a molecular solvation shell were obtained with Gaussian16 package[36]. Rubrene and PXZ-TRZ dissolved in toluene, chlorobenzene and dichloromethane with dielectric constant of 2.4, 5.6 and 9.1, respectively, are studied in this work. The multiconfigurational semiempirical DFT/MRCI-R method[37] was employed for calculation of excited-state properties with def-SV(P) atomic basis set and def-SV(P) auxiliary basis[38] for two-electron integral calculation using the tight set of the MRCI optimized parameters[37].

Fluorescence spectra of the donor and absorption spectra of the acceptor at different temperature intervals were determined using a time-dependent approach implemented in the VIBES program[39–41]. Light emission from the optically dark charge-transfer state of PXZ-TRZ requires transition dipole derivatives, which were determined numerically by distorting the S_1 geometry along non-totally symmetric normal coordinates yielding the Herzberg-Teller (HT) type of emission. The vibrationally induced *(x,y,z)*-components of the transition dipole were derived in its length representation form from the corresponding DFT/MRCI-R wave functions. Resulting elements, listed in the supplementary material, were used for the calculation of the interchromophore interaction and the HT fluorescence spectrum. For simplicity, we ignore the HT factor of the dipole-allowed absorption of Rubrene and rely solely on the Franck-Condon picture using theoretically adjusted geometry displacement parameters derived in reference[42]. To simulate the experimental spectral broadening, the Fourier transformation of the auto-correlation function was at-

tenuated by a Gaussian damping with a 250 cm^{-1} width at half-maximum.

The vibrational wave packet calculations were performed with the Heidelberg MCTDH package [43–45]. All discretized vibrational modes of the S_1 electronic potential of PXZ-TRZ were split into different layers, forming a highly contracted multi-layer (ML) structure of vibrational wave function [46–48]. Also we introduced a separate branch for the totally symmetric modes in the ML diagram, which leads to more accurate density redistribution at various thermal conditions. The ML-tree with five layer depths embraces all 174 nuclear degrees of freedom of PXZ-TRZ. The time-dependent single-particle functions of the physical degrees of freedom were described by the Hermite functions. The complete information about the MCTDH basis, structure of the ML-tree, the HT-coupling coefficients are found in the supplementary material. We carried out 300 ML-MCTDH relaxation jobs at every temperature interval to obtain the final vibrational state in the framework of the stochastic random wavefunction approach [49,50]. Consequently, the effective transition dipole moment of PXZ-TRZ represents an average over a number of stochastic realizations. A single element of the ensuing random-phase sample depicts a non-symmetric distribution of the vibration density with respect to the Franck-Condon point, contracted by different kinetic components peculiar to a nuclear displacement coordinate at fixed temperature (see supplementary material for details).

3 Results and discussions

3.1 Absorption and emission spectra

The Rubrene molecule has been studied for many years and been applied as a fluorescent dopant in OLEDs [24,51–53]. It is well known that the carbon framework of Rubrene can be arranged in two possible conformations which are characterized by D_{2h} and D_2 symmetry. The D_{2h} conformer exhibits a planar configuration of the tetracene backbone with perpendicularly oriented phenyl rings. In contrast, the D_2 structure twists the aromatic plane and therefore reorients the phenyl ligands. The latter twisted D_2 configuration is known to be energetically favorable in solution and thin film, while the D_{2h} structure dominates in a molecular bulk crystal [54,55]. Because the emissive layer of a device usually represents an amorphous solid of host molecules with a low dopant concentration, we used the D_2 conformer of Rubrene in this study.

The Rubrene molecule possesses a single, dipole allowed electronic band in the 2 eV energy region. Similar to the L_a state in the polyacene family, this $1^1A \rightarrow 1^1B_2$ electronic excitation involves one particle promotion from the highest occupied molecular orbital (HOMO) to the lowest unoccupied molecular orbital (LUMO) with vertical energy of 2.32 eV and oscillator strength of $f(L)$=0.26 in vacuum. In this study we did not observe any environment effect on the excited state energy of Rubrene according to the DFT/MRCI-R calculations (see Table 1). The HOMO and LUMO orbitals of Rubrene are mainly localized on the tetracene backbone as shown in Figure 1. The 1^1B_2 electronic configuration changes the π-conjugation such that nominally bonding p_z-orbitals of neighboring atoms in HOMO become antibonding in LUMO and *vice versa*. These electrostatic forces activate the nuclear motion of carbons, which stabilizes the $\pi\pi^*$ excited state energy. As the result, the absorption spectrum of Rubrene shows pronounced vibronic progression originating from geometric deformations of the C–C network as illustrated in Figure 2. The main vibronic features of the spectrum are well described by the activities of the 1372 cm^{-1} and 1521 cm^{-1} modes as the components with large normal displacements caused by the $1^1A \rightarrow 1^1B_2$ electronic transition. In addition, a set of low energy Franck-Condon (FC) modes with nonzero values of the excited-state displacement yields to a noticeable broadening for each of the overtones from the main progression series. In this study all displacement parameters and optimal frequencies were taken from the work by *Petrenko et al.*, which were obtained for the BHLYP geometry of Rubrene in order to reproduce the experimentally observed bandshape [42].

Table 1 Vertical and adiabatic transition energies of the monomers in eV.

	DFT/MRCI				Exp.
	VAC	TOL	CLB	DCM	
Rubrene					
$S_0 \rightarrow S_1$	2.32	2.32	2.32	2.32	2.36[a,b] 2.37[c] 2.33[d]
$S_1 \rightarrow S_0$	2.09	2.09	2.09	2.09	2.25[e] 2.23[f]
E_{ad}	2.20	2.20	2.20	2.20	
PXZ-TRZ					
$S_0 \rightarrow S_1$	2.85	2.92	2.95	2.96	2.95[g] 2.92[h]
$S_1 \rightarrow S_0$	2.33	1.65	1.25	1.14	2.30[k,l] 2.25[m] 2.36[n]
E_{ad}	2.58	1.87	1.47	1.34	

[a] absorption maximum in acetone from Ref. [56]
[b] absorption maximum in toluene from Ref. [57]
[c] absorption maximum in hexane from Ref. [58]
[d] absorption maximum in pyridine from Ref. [58]
[e] emission maximum in cyclohexane from Ref. [42]
[f] emission maximum in toluene from Ref. [57]
[g] absorption maximum in toluene from Ref. [59]
[h] absorption maximum in toluene from Ref. [60]
[k] emission maximum in mCBP matrix from Ref. [61]
[l] emission maximum in CPCN matrix from Ref. [60]
[m] emission maximum in toluene solvent from Ref. [59]
[n] emission maximum in 2-MeTHF from Ref. [59]

Fig. 2 Rubrene absorption and PXZ-TRZ emission spectra at 300K.

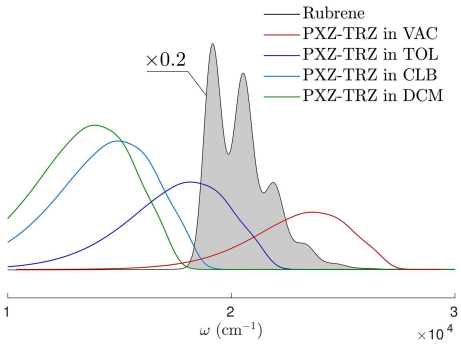

The PXZ-TRZ dye consists of phenoxazine and triphenyltriazine moieties with perpendicularly oriented π-planes which are weakly coupled together by the covalent carbon-nitrogen bond. In the event of charge carrier recombination, the electronic con-

figuration undergoes the HOMO→LUMO electron-transfer excitation, where the HOMO resides on phenoxazine donor and the LUMO on the triphenyltriazine electron acceptor (Figure 1). Both the S_0 and S_1 nuclear configurations of PXZ-TRZ possess the C_{2v} point group symmetry. As is typical for the bichromophoric TADF systems, the radiation emission occurs from the initially populated CT state, which is optically dark in nature at the S_1 minimum. This entails a breakdown of the Condon approximation and necessitates a thorough examination of non-symmetric vibrational modes[62,63]. Furthermore, because the charge-transfer state possesses a large dipole moment, which is oriented anti-collinear to that of the ground state, the effects of solute-solvent polarization play an important role. As it was emphasized in previous theoretical works on OLEDs[64,65], the sub-microsecond prompt fluorescence is equivalent to the characteristic time scale of solvent reorganization supervening the exciton formation even in confined conditions of amorphous solids. This causes instability of the emission peak over the transient fluorescence time[66,67]. However, the framework of the Förster exciton transfer suggests a static picture of radiation emission, and we adapted the reaction field optimized for the CT state to simulate the steady-state fluorescence spectrum of PXZ-TRZ. Table 1 shows the vertical excitation and de-excitation energies for the lowest singlet excited state in different environments. In contrast to Rubrene, where the S_1 state energy appears inert to the medium, the static permittivity of the solvent stabilizes the S_1 energy of PXZ-TRZ with respect to the ground state. By virtue of large dipole moment of the CT state, the calculated $1^1A_2 \rightarrow 1^1A_1$ electronic de-excitation energy is substantially lowered with increasing solvent polarity as given in Table 1. The most prominent nuclear displacement of the 1^1A_2 geometry with respect to the 1^1A_1 state is due to two vibrational coordinates with frequencies of 421 cm^{-1} and 1681 cm^{-1}. They characterize the coupled C–O–C and C–N–C bending of the phenoxazine fragment and elongation of the C–N bond linking the chromophores. The aforementioned FC modes constitute a vibronic progression of the fluorescence spectrum of PXZ-TRZ provided that the non-totally symmetric modes generate non-zero oscillator strength.

Because the FC point of the emissive CT state sets PXZ-TRZ in C_{2v} symmetry we use the symmetry-related principle to unravel the combined electron-nuclear problem of light emission and exciton hopping. The Figure 3 graphically shows the transition dipole moment derivatives with respect to the a_2 nuclear distortions peculiar to the S_1 potential energy surface. These low-temperature vibrations describe twisting and wagging of the electron donor moiety and of the phenyl ring encapsulated between the phenoxazine and triazine fragments. Their interplay with the totally symmetric a_1 modes results in a broad-shaped fluorescence spectrum of PXZ-TRZ with solvent-dependent peak maximum, which is red shifted upon increase of the dielectric constant of medium. We also note that the magnitude of the transition dipole derivatives is increased with increasing solvent polarity, which explains the balance of relative intensity of the TADF emission spectra in Figure 2.

Fig. 3 Transition dipole derivative with respect to the a_2-normal displacements (q_1, q_9, ...) in different solvents.

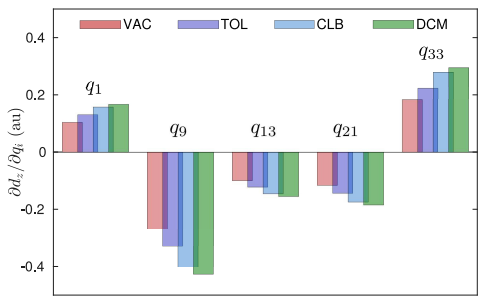

The ET rate k_{ET} crucially depends on the relative position of spectral band structure of donor and acceptor acknowledged in the overlap integral S:

$$k_{ET} = \frac{2\pi\kappa^2}{\hbar R^6} \int S_a(\omega) S_d(\omega) d\omega \qquad (4)$$

where S_a and S_d are the absorption and emission bandshapes of the respective monomers explicitly (in case of the FC-type) or implicitly (in case of the HT-type) encoding the transition dipole moments[28,29,68]. We blueshift the calculated fluorescence spectrum of PXZ-TRZ in toluene at 300K to fit the intensity peak with the experimental position at 2.25 eV[59]. Assuming that a source of this correction changes the $S_1 \rightarrow S_0$ energy in all solvents by the constant interval, we adjust the spectral onset of all models accordingly. In this respect the relative positions of the PXZ-TRZ fluorescence maxima in different environments remain unaltered. For example, the ~0.4 eV gap between the peaks in toluene and chlorobenzene is well correlated with the observed ~0.3 eV energy shift in structurally almost identical DMAC-TRZ dye[60]. In the same way the blue shift was introduced for the absorption spectrum of Rubrene in toluene, which matches the theoretical outcome with the measurements[57].

3.2 Energy transfer

In a double-dopant device, the initial singlet excitons on TADF molecules have two possible ways for the radiative recombination. The first way is the radiative decay from the TADF molecule itself with characteristic rate constant of 10^{6-8} s^{-1} for a donor-acceptor system. Another route involves the S_1 state of a fluorophore for non-radiative ET followed by light emission from the highly luminescent state. Whilst the former is described solely by intramolecular electronic properties of the TADF molecule, the latter process crucially depends on the interchromophore distance R and their mutual orientation in space defined by orientational parameter κ. The orientation κ comprises the relative alignment of the transition dipoles of monomers and varies between $0 \leq \kappa^2 \leq 4$. The exciton transfer efficiency between PXZ-TRZ and Rubrene can be controlled by these two largest contributing factors.

The radiative lifetime τ_F of the singlet PXZ-TRZ exciton results from integration of the HT spectral density over frequency domain[69]:

$$\frac{1}{\tau_F} = \frac{4}{3\hbar c^3} \int \omega^3 S_d(\omega) d\omega \qquad (5)$$

The computed emission lifetime in toluene at 300K is $\tau_F = 109$ ns. The transient photoluminescence decay of PXZ-TRZ at the same ambient condition revealed 19 ns for the prompt component and 0.67 μs for the delayed component with the photoluminescence quantum yield of 29.5%[59]. Because the equation 5 assumes absence of non-radiative decay channels, i.e. that 100% of the singlet exciton is transmitted into radiation emission, our computed τ_F overshoots a pure radiative decay time by factor not higher than 1.8. At lower temperature regimes the activity of the dipole-coupling modes are more confined and the τ_F becomes longer, as summarized in Table 2. In order to suppress light emission on the PXZ-TRZ sensitizer by efficient exciton transfer, the critical intermolecular distance at a certain monomeric orientation κ must comply with the following expression:

$$R = \left(\frac{2\pi}{\hbar}\kappa^2 S \Big/ k_F\right)^{1/6} \quad (6)$$

which is well known as Förster radius. The term S in Equation 6 is the spectral overlap integral from Equation 4 ensuring energy conservation upon the exciton hopping, and k_F is the fluorescence rate of energy donor. Because the overlap S includes the integration over the emission shape of PXZ-TRZ, a possible error of the computed fluorescence lifetime is partly canceled in the expression for the Förster radius. Assuming that the orientation of Rubrene and PXZ-TRZ is not controlled during the deposition on a substrate, the random orientation factor κ^2 returns $2/3$. In this case the critical interchromophore distance for one donor-acceptor pair is about 5.5-6 nm in toluene solution. Due to the red-shift of the TADF fluorescence in chlorobenzene and acetonitrile, the spectral overlap becomes very small and efficient exciton energy transfer requires close contact between monomers (see Table 2). Nakanotani et al.[24] provide 6.9 nm as an estimate of Förster radius for the same dyad co-doped in a mCBP matrix, which is close to our computed values.

Fig. 4 (a) Oscillations of the components of the transition dipole moments of PXZ-TRZ in vacuum at 300K. (b) Running average of the transition dipole moment of PXZ-TRZ in vacuum with respect to the number of stochastic realizations.

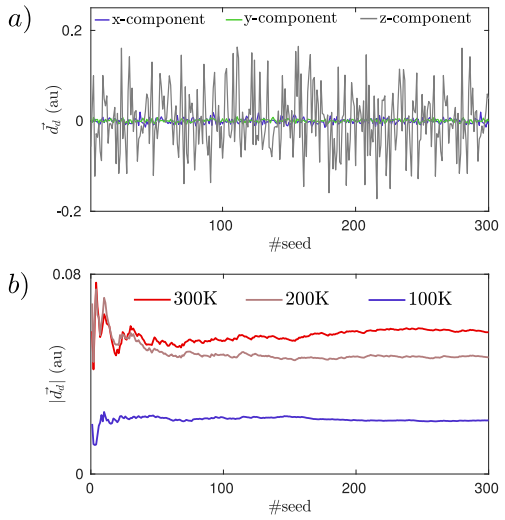

In FRET-based devices, excitons are desired to be generated preferentially on the TADF molecules which pave the way for harvesting triplet excitons via rISC. This is usually achieved by low concentration of fluorophores as compared with the concentration of the carrier recombination centers. Thereby, operational control of the relative orientation of the dopants is a key criterion for efficient ET keeping the mesoscopic parameters of emission layer constant. The main obstacle in transfer modelling originates from the fact that the CT state of conventional TADF systems either does not possess a static transition dipole moment to the ground state or that the moment is very small, which is usually observed in TADF molecules having a low degree of spatial symmetry. By analogy to the rISC mechanism, both the radiation emission and the competing ET are vibrationally driven processes. In this regard, the preferential alignment of chromophores relies on the principal axis of the vibrationally induced transition dipole moment of PXZ-TRZ. We adapt the one-state vibrational ML-MCTDH Hamiltonian peculiar to the S_1 electronic potential of PXZ-TRZ in order to shed light on the nature of the transition moment associated with molecular vibrations. Figure 4-a displays the thermal fluctuation of the Cartesian component of the transition dipole at 300K resulting from different realizations of the random-phase nuclear wavefunction. It is clearly seen that the oscillations along the molecular z-axis occur with much higher amplitude than along the x- and y- coordinates. Although all components of $\vec{d}$ converge to zero after averaging over the entire sample, the absolute value of the vector converges to a non-zero value at each temperature interval as illustrated in Figure 4-b. Moreover, the $|\vec{d}|$ is dominated by its z-component by not less than 98% in all solute-solvent models considered in this work. We interpret this outcome as the result of strong adiabating mixing between the optically forbidden CT state and the first excited local $\pi\pi^*$ state of $^1A_1$ symmetry at the FC point of the S_1 state. This bright exciton resides mainly on triphenyltriazine moiety of PXZ-TRZ and possesses large oscillator strength. The a_2 nuclear distortions mediate the vibronic coupling between 2^1A_1 and 1^1A_2 states as a result of which the CT state borrows the intensity for radiative exciton recombination. This outcome suggests an optimal relative orientation of the PXZ-TRZ and Rubrene molecular frames for enhancing the efficiency of the ET process. If the transition moment of Rubrene lines up along the intrinsic z-axis of PXZ-TRZ, the κ^2 coefficient reaches its superior limit of 4, which corresponds to the fastest non-radiative depopulation of the CT state. Based on this alignment, we compute the ultimate Förster distance R_{max} between the chromophores as listed in Table 2. It is known from experiments that the spatial orientation of light emitting molecules, whose transition dipole moment is aligned horizontally to the glass substrate, enhances the light out-coupling efficiency of the OLED.[70–73] Komino et al.[61] have demonstrated that the horizontal orientation of PXZ-TRZ dopants in randomly oriented mCBP host matrix increase of the external efficiency of a device by 24%. This experimental evidence corroborates our finding that the transition dipole moment of PXZ-TRZ fluctuates in-plane.

Table 2 The ET related parameter for PXZ-TRZ/Rubrene dimer: τ_F – the radiative lifetime of PXZ-TRZ; S – spectral overlap of the PXZ-TRZ emission and the Rubrene absorption; R_{aver} – Förster radius for randomly oriented monomers; R_{max} – Förster radius for the monomers alignment as shown in Figure 5.

	VAC			TOL			CLB			DCM		
	100K	200K	300K	100K	200K	300K	100K	200K	300K	100K	200K	300K
τ_F (ns)	149	95	72	216	140	109	253	168	134	276	185	148
S (au)	8.5	21	41	51	73	79	4.0	2.8	2.8	<0.1	<0.1	0.8
R_{aver} (nm)	4.1	4.4	4.7	5.9	5.8	5.7	4.0	3.5	3.4	1.3	1.6	2.7
R_{max} (nm)	5.5	6.0	6.4	7.9	7.8	7.6	5.3	4.7	4.5	1.8	2.2	3.7

3.3 Mutual orientation of dopants

The combination of Rubrene and PXZ-TRZ perfectly demonstrates a potential scheme for enhancing the efficiency of the TADF-operating OLEDs. The idea relies on the mutual alignment of the interacting chromophores, and therefore knowledge of the principal $S_1 \rightarrow S_0$ transition dipole axis of a TADF molecule is the primary task. As we pointed out before, this question is not always easy to answer because of the dark nature of the CT state. It especially concerns a family of linear-shaped cassettes where the FC-type fluorescence is forbidden by the symmetry constraints. In this case the molecular vibrations can bring non-zero probability for light emission manifesting the Jahn-Teller phenomena. A rigorous study of all TADF candidates and characterization of intramolecular interstate vibronic couplings would be computationally laborous. However, this exhaustive analysis can be avoided under certain circumstances, i.e. when an electronic excitation spectrum of the TADF molecule at the S_1 geometry reveals high-intensity bands of a certain type of dipole symmetry. Below, we provide some guiding principles with illustrative examples of the preferential morphology of a linear shaped TADF molecule and a complementary fluorescent partner. In the following discussion we refer the reader to Figure 5.

The proper combination of exciton acceptor and exciton donor is commonly realized as a rapid resonance energy transfer requiring substantial spectral overlap S. A rather large Stoke shift of the TADF molecule prohibits the back energy transfer from a fluorophore to TADF, which should possess a bright one-photon transition in the energy region of a TADF emission. The light emission from energy-acceptor systems without long vibronic progression seems ideal for obtaining high color purity of hyperfluorescence. Further, a substantial energy separation between the emitting S_1 state and other local excitations on a fluorophore can minimize losses upon the relaxation, and increase the internal efficiency of an OLED. As recently shown[24], a family of rigid polycyclic aromatic compounds with dipole allowed $\pi\pi^*$ S_1 state can serve as optimal exciton recombination centers. The PXZ-TRZ dye deposited in mCBP host yields 12.8% of external electroluminescence quantum efficiency (EQE)[74]. Incorporation of a Rubrene derivative TBRb in the same matrix as an ET partner to PXZ-TRZ enhances the EQE by up to 18% and increases the device reliability almost by factor of 2[24]. Therefore, the operational control of orientational morphology of TBRb and PXZ-TRZ can enhance the reported performance of a device due to different means: (1) reducing the concentration of TBRb centers, which helps to rule out the charge carrier recombination on the fluorophore by that avoiding the triplet excitons trapping; (2) increasing the rate of exciton transport k_{ET}, which alleviates the triplet-to-singlet up-conversion dynamics on TADF centers; (3) producing the stable-over-time fluorescence signal achieved through apolar $\pi\pi^*$ state of TBRb. Further examples following the same general working principles are given below.

The green ACRFLCN dye consists of acridine donor that is spiro-conjugated to fluorene acceptor. An OLED with ACRFLCN doped in TPSi-F host achieves nowadays modest 10% EQE[75]. The maximum electroluminescence intensity at 485 nm originates from vibronic interaction of the CT state with the local $\pi\pi^*$ exciton residing on the fluorene unit. The relatively large oscillator strength $f(L)$=1.1 of the fluorene monomer extends almost equally across the first two B_2 transitions in ACRFLCN, suggesting the molecular y-axis for alignment of an emitter. The TPA molecule is one of the diaminoanthracene derivatives, displaying an excitation peak at 456 nm and 526 nm emission with quantum yield of 0.83 measured in dichloromethane, optimal for ACRFLCN[76]. Similar to the $S_0 \rightarrow S_1$ transition in Rubrene, this electronic configuration with $f(L)$=0.26 involves HOMO-LUMO electron promotion with the underlying orbitals localized mainly on the anthracene backbone. Utilizing TPA in the role of fluorescent partner to ACRFLCN in an emissive layer can bring high brightness green light.

The electroluminescence of the donor-acceptor-donor PTZ-DBPHZ-PTZ system with two conformationally switchable phenothiazine units peaks at 587 nm in blended CBP film[77]. The performance of the reported orange-color device reaches up to 17% of EQE, indicating that the PTZ-DBPHZ-PTZ is an efficient exciton sensitizer. According to the DFT/MRCI calculations, the local dibenzophenazine excitons at 3.00 eV and 4.09 eV with 0.37 and 2.05 oscillator strength, respectively, prevail in the electronic excitation spectrum at the CT geometry. The emissive S_1 state inherits its dipole moment upon molecular vibrations around the FC point. Terrylene is a deep-red compound with small Stoke shift displaying maximum absorption intensity at 560 nm and emission wavelength at 575 and 612 nm[78]. Its fluorescence quantum yield is close to unity with no notable transition to the triplet manifold.[79] A high photostability renders terrylene as good fluorescent partner to PTZ-DBPHZ-PTZ.

A TADF emitter SpiroAC-TRZ, built from a spiroacridine donor covalently linked electron-accepting triazine unit, exhibits sky-blue electroluminescence with maximum spectral intensity at 480 nm[80]. Remarkably, the horizontal orientation of planar SpiroAC-TRZ with respect to the substrate boosts the outcoupling efficiency as compared with blended morphology of an emissive layer mimicking the strong anisotropy of the transition dipole. Overall, an ultimate EQE of 36.7% can be achieved by virtue of the outcou-

Fig. 5 The preferential alignment of TADF molecules to their complementary fluorescent partners for maximizing the ET efficiency. The localization of the optically bright excitons on the assistant dopants is schematically highlighted in red-shaded region. The spectral intensity and energetic position of the ET driving excitons are given on the bottom bars with illustration of the underlying electron-hole pair density.

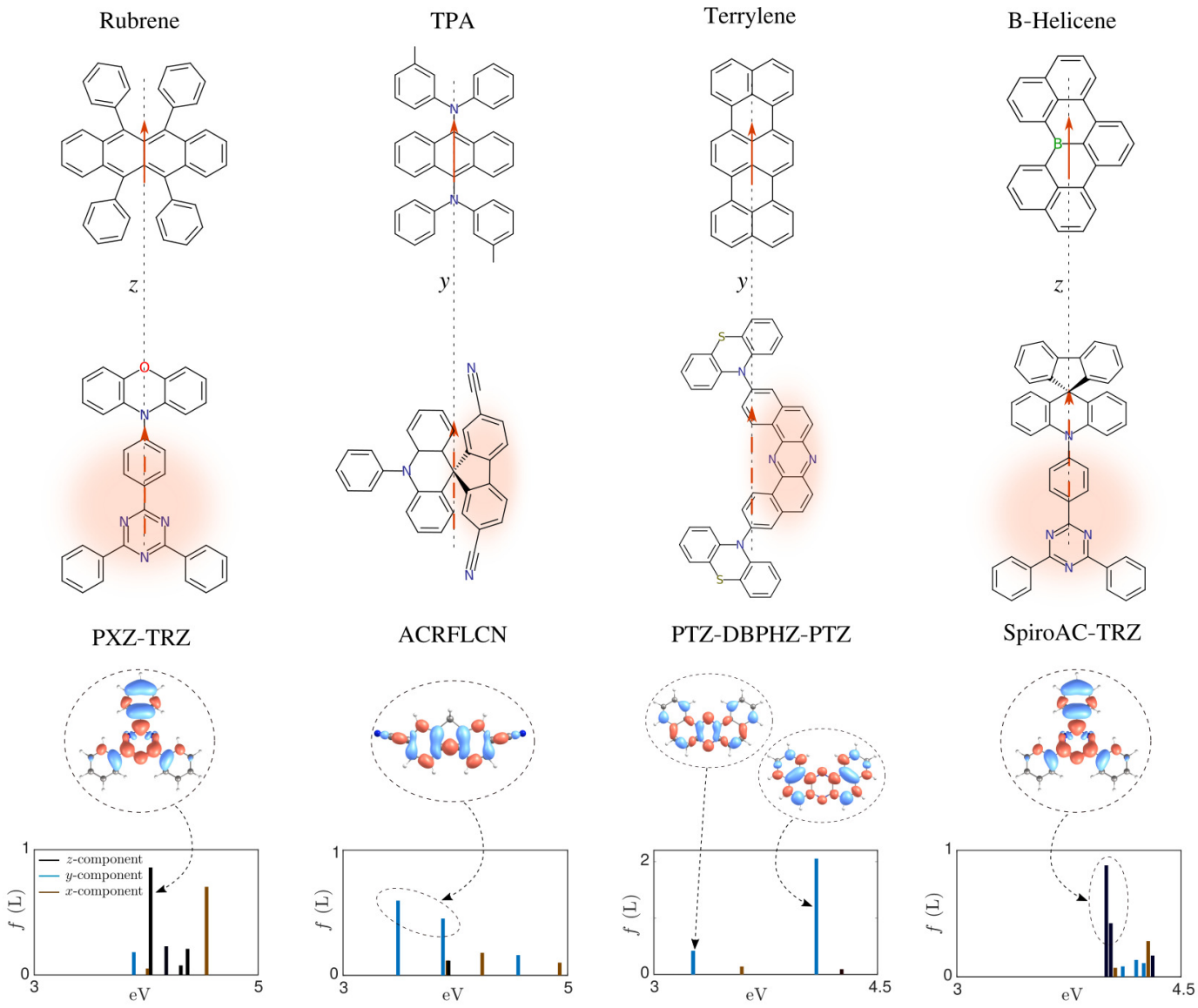

pling enhancing technologies and employing a mCPCN host material[80]. The lowest bright excited states with large z-component of the transition dipole arise due to intensity distribution of the $\pi\pi^*$ exciton residing on the triphenyltriazine fragment. The CT state borrows the intensity from the bright exciton causing the experimentally observed in-plane emission. A possible way to achieve hyperfluorescence utilizing SpiroAC-TRZ as exciton sensitizer is a co-deposition of a boron-containing Helicene (B-Helicene). The first optically bright transition at 466 nm of the B-Helicene diluted in C_6H_6 stems[81] from the interaction of frontier HOMO-LUMO π-orbitals. Its spectral density of light emission displays a pronounced vibronic structure placing the overtones at 493 and 525 nm and yielding 75% of quantum efficiency.[81] The extremely efficient triplet-harvesting ability of SpiroAC-TRZ and the excellent solubility of B-Helicene suggests a potentially remarkable ET pair for a green-light device.

4 Conclusions

In this paper we described the singlet exciton transfer from the PXZ-TRZ molecule to the highly luminescent Rubrene. Similar to the primary step of rISC mechanism in TADF, the vibronic interaction between electronically excited states in linear shaped TADF molecules plays the key role in generation of non-zero electronic transition dipole moment. The knowledge of the principal molecular axis of the fluctuating transition dipole paves a way for designing full-color OLEDs with outstanding efficiency and improved operational stability. We emphasize the importance of the nature of low-energy lying singlet excited states for the radiative exciton recombination on TADF center in single-dopant OLEDs and for the non-radiative exciton transfer from TADF to fluorophore in double-dopant OLEDs.

Conflicts of interest

There are no conflicts to declare.

Acknowledgements

This work was supported by the Australian Government through the Australian Research Council (ARC) under the Centre of Excellence scheme (project number CE170100026) and by Deutsche Forschungsgemeinschaft (DFG) through project MA1051/17-1. It was also supported by computational resources provided by the Australian Government through the National Computational Infrastructure National Facility and the Pawsey Supercomputer Centre.

Notes and references

1 H. Uoyama, K. Goushi, K. Shizu, H. Nomura and C. Adachi, Nature, 2012, **492**, 234.
2 F. B. Dias, K. N. Bourdakos, V. Jankus, K. C. Moss, K. T. Kamtekar, V. Bhalla, J. Santos, M. R. Bryce and A. P. Monkman, Adv. Mater., 2013, **25**, 3707–3714.
3 Y. Tao, K. Yuan, T. Chen, P. Xu, H. Li, R. Chen, C. Zheng, L. Zhang and W. Huang, Adv. Mater., 2014, **26**, 7931–7958.
4 M. Godumala, S. Choi, M. J. Cho and D. H. Choi, J. Mater. Chem. C, 2016, **4**, 11355–11381.
5 M. Y. Wong and E. Zysman-Colman, Adv. Mater., 2017, **29**, 1605444.
6 Z. Yang, Z. Mao, Z. Xie, Y. Zhang, S. Liu, J. Zhao, J. Xu, Z. Chi and M. P. Aldred, Chem. Soc. Rev., 2017, **46**, 915–1016.
7 Y. Li, J.-Y. Liu, Y.-D. Zhao and Y.-C. Cao, Mater. Today, 2017, **20**, 258–266.
8 Y. Im and J. Y. Lee, J. Inf. Disp., 2017, **18**, 101–117.
9 J. Gibson, A. P. Monkman and T. J. Penfold, ChemPhysChem, 2016, **17**, 2956–2961.
10 M. K. Etherington, J. Gibson, H. F. Higginbotham, T. J. Penfold and A. P. Monkman, Nat. Commun., 2016, **7**, 13680.
11 C. M. Marian, J. Phys. Chem. C, 2016, **120**, 3715–3721.
12 T. J. Penfold, E. Gindensperger, C. Daniel and C. M. Marian, Chem. Rev., 2018, DOI: 10.1021/acs.chemrev.7b00617.
13 S. Scholz, D. Kondakov, B. Lüssem and K. Leo, Chem. Rev., 2015, **115**, 8449–8503.
14 S. Reineke, K. Walzer and K. Leo, Phys. Rev. B, 2007, **75**, 125328.
15 M. A. Baldo, C. Adachi and S. R. Forrest, Phys. Rev. B, 2000, **62**, 10967–10977.
16 A. S. D. Sandanayaka, T. Matsushima and C. Adachi, J. Phys. Chem. C, 2015, **119**, 23845–23851.
17 S. Wook and L. J. Yeob, Adv. Opt. Mater., 2017, **5**, 1600901.
18 K. Masui, H. Nakanotani and C. Adachi, Org. Electron., 2013, **14**, 2721–2726.
19 C. Li, L. Duan, D. Zhang and Y. Qiu, ACS Appl. Mater. Interfaces, 2015, **7**, 15154–15159.
20 B. Zhao, T. Zhang, B. Chu, W. Li, Z. Su, H. Wu, X. Yan, F. Jin, Y. Gao and C. Liu, Sci. Rep., 2015, **5**, 10697.
21 C.-C. Lin, M.-J. Huang, M.-J. Chiu, M.-P. Huang, C.-C. Chang, C.-Y. Liao, K.-M. Chiang, Y.-J. Shiau, T.-Y. Chou, L.-K. Chu, H.-W. Lin and C.-H. Cheng, Chem. Mater., 2017, **29**, 1527–1537.
22 D. Zhang, C. Zhao, Y. Zhang, X. Song, P. Wei, M. Cai and L. Duan, ACS Appl. Mater. Interfaces, 2017, **9**, 4769–4777.
23 T. C. Wu, D. N. Congreve and M. A. Baldo, Appl. Phys. Lett., 2015, **107**, 031103.
24 H. Nakanotani, T. Higuchi, T. Furukawa, K. Masui, K. Morimoto, M. Numata, H. Tanaka, Y. Sagara, T. Yasuda and C. Adachi, Nat. Commun., 2014, **5**, 4016.
25 T. Furukawa, H. Nakanotani, M. Inoue and C. Adachi, Sci. Rep., 2015, **5**, 8429.
26 H. Fukagawa, T. Shimizu, Y. Iwasaki and T. Yamamoto, Sci. Rep., 2017, **7**, 1735.
27 D. Zhang, L. Duan, C. Li, Y. Li, H. Li, D. Zhang and Y. Qiu, Adv. Mater., 2014, **26**, 5050–5055.
28 V. May and O. Kühn, Charge and Energy Transfer Dynamics in Molecular Systems, Wiley-VCH Verlag GmbH, 2007, pp. 404–477.
29 S. Banerjee, A. Baiardi, J. Bloino and V. Barone, J. Chem. Theory Comput., 2016, **12**, 2357–2365.
30 TURBOMOLE v7.2 2017, a development of University of Karlsruhe and Forschungszentrum Karlsruhe GmbH, 1989-2007, TURBOMOLE GmbH, since 2007; available from http://www.turbomole.com.
31 A. D. Becke, J. Chem. Phys., 1993, **98**, 1372–1377.
32 A. Schäfer, H. Horn and R. Ahlrichs, J. Chem. Phys., 1992, **97**, 2571–2577.
33 S. Grimme, J. Antony, S. Ehrlich and H. Krieg, J. Chem. Phys., 2010, **132**, 154104.
34 J. Neugebauer, M. Reiher, C. Kind and B. A. Hess, J. Comput. Chem., 2002, **23**, 895–910.
35 M. Caricato, B. Mennucci, J. Tomasi, F. Ingrosso, R. Cammi, S. Corni and G. Scalmani, J. Chem. Phys., 2006, **124**, 124520.
36 M. J. Frisch, G. W. Trucks, H. B. Schlegel, G. E. Scuseria, M. A. Robb, J. R. Cheeseman, G. Scalmani, V. Barone, G. A. Petersson, H. Nakatsuji, X. Li, M. Caricato, A. V. Marenich, J. Bloino, B. G. Janesko, R. Gomperts, B. Mennucci, H. P. Hratchian, J. V. Ortiz, A. F. Izmaylov, J. L. Sonnenberg, Williams, F. Ding, F. Lipparini, F. Egidi, J. Goings, B. Peng, A. Petrone, T. Henderson, D. Ranasinghe, V. G. Zakrzewski, J. Gao, N. Rega, G. Zheng, W. Liang, M. Hada, M. Ehara, K. Toyota, R. Fukuda, J. Hasegawa, M. Ishida, T. Nakajima, Y. Honda, O. Kitao, H. Nakai, T. Vreven, K. Throssell, J. A. Montgomery Jr., J. E. Peralta, F. Ogliaro, M. J. Bearpark, J. J. Heyd, E. N. Brothers, K. N. Kudin, V. N. Staroverov, T. A. Keith, R. Kobayashi, J. Normand, K. Raghavachari, A. P. Rendell, J. C. Burant, S. S. Iyengar, J. Tomasi, M. Cossi, J. M. Millam, M. Klene, C. Adamo, R. Cammi, J. W. Ochterski, R. L. Martin, K. Morokuma, O. Farkas, J. B. Foresman and D. J. Fox, Gaussian 16 Rev. B.01, 2016.
37 I. Lyskov, M. Kleinschmidt and C. M. Marian, J. Chem. Phys., 2016, **144**, 034104.
38 K. Eichkorn, O. Treutler, H. Öhm, M. Häser and R. Ahlrichs, Chem. Phys. Lett., 1995, **240**, 283–290.

39 M. Etinski, J. Tatchen and C. M. Marian, J. Chem. Phys., 2011, **134**, 154105.

40 M. Etinski, V. Rai-Constapel and C. M. Marian, J. Chem. Phys., 2014, **140**, 114104.

41 M. Etinski, J. Tatchen and C. M. Marian, Phys. Chem. Chem. Phys., 2014, **16**, 4740–4751.

42 T. Petrenko, O. Krylova, F. Neese and M. Sokolowski, New J. Phys., 2009, **11**, 015001.

43 H.-D. Meyer, U. Manthe and L. S. Cederbaum, Chem. Phys. Lett., 1990, **165**, 73–78.

44 M. H. Beck, A. Jäckle, G. A. Worth and H.-D. Meyer, Phys. Rep., 2000, **324**, 1–105.

45 G. A. Worth, M. H. Beck, A. Jäckle and H.-D. Meyer, The MCTDH Package, Version 8.2, (2000), University of Heidelberg, Heidelberg, Germany. H.-D. Meyer, Version 8.3 (2002), Version 8.4 (2007). O. Vendrell and H.-D. Meyer, Version 8.5 (2011). See http://mctdh.uni-hd.de.

46 H. Wang and M. Thoss, J. Chem. Phys., 2003, **119**, 1289–1299.

47 H.-D. Meyer and G. A. Worth, Theor. Chem. Acc., 2003, **109**, 251–267.

48 O. Vendrell and H.-D. Meyer, J. Chem. Phys., 2011, **134**, 044135.

49 M. Nest and R. Kosloff, J. Chem. Phys., 2007, **127**, 134711.

50 D. Mendive-Tapia, T. Firmino, H.-D. Meyer and F. Gatti, Chem. Phys., 2017, **482**, 113 – 123.

51 H. Mattoussi, H. Murata, C. D. Merritt, Y. Iizumi, J. Kido and Z. H. Kafafi, J. Appl. Phys., 1999, **86**, 2642–2650.

52 Z. Wang, S. Naka and H. Okada, Appl. Phys. A, 2010, **100**, 1103–1108.

53 T.-Y. Chu, J.-F. Chen, S.-Y. Chen and C. H. Chen, Appl. Phys. Lett., 2006, **89**, 113502.

54 D. Käfer, L. Ruppel, G. Witte and C. Wöll, Phys. Rev. Lett., 2005, **95**, 166602.

55 K.-Y. Lin, Y.-J. Wang, K.-L. Chen, C.-Y. Ho, C.-C. Yang, J.-L. Shen and K.-C. Chiu, Sci. Rep., 2017, **7**, 40824.

56 M. Kytka, L. Gisslen, A. Gerlach, U. Heinemeyer, J. Kovác, R. Scholz and F. Schreiber, J. Chem. Phys., 2009, **130**, 214507.

57 L. Ma, K. Zhang, C. Kloc, H. Sun, M. E. Michel-Beyerle and G. G. Gurzadyan, Phys. Chem. Chem. Phys., 2012, **14**, 8307–8312.

58 G. Badger and R. Pearce, Spectrochim. Acta, 1951, **4**, 280–283.

59 H. Tanaka, K. Shizu, H. Miyazaki and C. Adachi, Chem. Commun., 2012, **48**, 11392–11394.

60 W.-L. Tsai, M.-H. Huang, W.-K. Lee, Y.-J. Hsu, K.-C. Pan, Y.-H. Huang, H.-C. Ting, M. Sarma, Y.-Y. Ho, H.-C. Hu, C.-C. Chen, M.-T. Lee, K.-T. Wong and C.-C. Wu, Chem. Commun., 2015, **51**, 13662–13665.

61 T. Komino, H. Tanaka and C. Adachi, Chem. Mater., 2014, **26**, 3665–3671.

62 I. Lyskov and C. M. Marian, J. Phys. Chem. C, 2017, **121**, 21145–21153.

63 J.-M. Mewes, Phys. Chem. Chem. Phys., 2018, **20**, 12454–12469.

64 T. Northey, J. Stacey and T. J. Penfold, J. Mater. Chem. C, 2017, **5**, 11001–11009.

65 J. Föller and C. M. Marian, J. Phys. Chem. Lett., 2017, **8**, 5643–5647.

66 F. B. Dias, J. Santos, D. R. Graves, P. Data, R. S. Nobuyasu, M. A. Fox, A. S. Batsanov, T. Palmeira, M. N. Berberan-Santos, M. R. Bryce and A. P. Monkman, Adv. Sci., 2016, **3**, 1600080.

67 G. Méhes, K. Goushi, W. J. Potscavage and C. Adachi, Org. Electron., 2014, **15**, 2027–2037.

68 J. D. Spiegel, M. Kleinschmidt, A. Larbig, J. Tatchen and C. M. Marian, J. Chem. Theory Comput., 2015, **11**, 4316–4327.

69 S. Banerjee, A. Baiardi, J. Bloino and V. Barone, J. Chem. Theory Comput., 2016, **12**, 774–786.

70 D. Yokoyama, J. Mater. Chem., 2011, **21**, 19187–19202.

71 T. D. Schmidt, D. S. Setz, M. Flämmich, J. Frischeisen, D. Michaelis, B. C. Krummacher, N. Danz and W. Brütting, Appl. Phys. Lett., 2011, **99**, 163302.

72 L. Zhao, T. Komino, M. Inoue, J.-H. Kim, J. C. Ribierre and C. Adachi, Appl. Phys. Lett., 2015, **106**, 063301.

73 D. H. Kim, K. Inada, L. Zhao, T. Komino, N. Matsumoto, J. C. Ribierre and C. Adachi, J. Mater. Chem. C, 2017, **5**, 1216–1223.

74 H. Tanaka, K. Shizu, H. Nakanotani and C. Adachi, Chem. Mater., 2013, **25**, 3766–3771.

75 G. Méhes, H. Nomura, Q. Zhang, T. Nakagawa and C. Adachi, Angew. Chem. Int. Ed., 2012, **51**, 11311–11315.

76 M.-X. Yu, J.-P. Duan, C.-H. Lin, C.-H. Cheng and Y.-T. Tao, Chem. Mater., 2002, **14**, 3958–3963.

77 M. Okazaki, Y. Takeda, P. Data, P. Pander, H. Higginbotham, A. P. Monkman and S. Minakata, Chem. Sci., 2017, **8**, 2677–2686.

78 R. Rieger and K. Müllen, J. Phys. Org. Chem., 2010, **23**, 315–325.

79 Y. Avlasevich, C. Kohl and K. Müllen, J. Mater. Chem., 2006, **16**, 1053–1057.

80 L. Ting-An, C. Tanmay, T. Wei-Lung, L. Wei-Kai, W. Meng-Jung, J. Min, P. Kuan-Chung, Y. Chih-Lung, C. Chin-Lung, W. Ken-Tsung and W. Chung-Chih, Adv. Mater., 2016, **28**, 6976–6983.

81 K. Schickedanz, T. Trageser, M. Bolte, H.-W. Lerner and M. Wagner, Chem. Commun., 2015, **51**, 15808–15810.

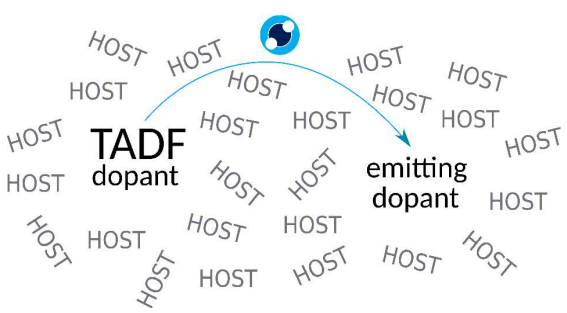
HOST
TADF
dopant
emitting
dopant

A role of mutual orientation of thermally activated delayed fluorescence dopants and their complementary fluorophores in organic light emitting diodes.